IOP Publishing Inverse Problems

Inverse Problems **34** (2018) 085009 (28pp) https://doi.org/10.1088/1361-6420/aac520

A Biot model for the determination of material parameters of cancellous bone from acoustic measurements

Hua Chen[1], **Robert P Gilbert**[2] **and Philippe Guyenne**[1]

[1] Department of Mathematical Sciences, University of Delaware, Newark, DE 19716, United States of America
[2] Institute of Mechanics and Materials, Ruhr–Universität Bochum, 44801 Bochum, Germany

E-mail: guyenne@udel.edu

Received 14 October 2017, revised 8 May 2018
Accepted for publication 16 May 2018
Published 27 June 2018

Abstract

A numerical investigation is presented for the feasibility of determining material parameters of cancellous bone by acoustic interrogation in two dimensions. A mathematical formulation is proposed for the *in vitro* experiment where a bone sample is immersed in a rectangular water tank. Modified Biot's equations for cancellous bone are coupled with a boundary integral equation for the water pressure. Cancellous bone is described as an isotropic and homogeneous medium with constant material parameters. An explicit expression for the Green's function is derived in the form of a double series. Well-posedness is established for a variational formulation of this nonlocal boundary value problem. Sensitivity and recovery tests are performed for frequencies in the ultrasonic range, and the results show that such parameters as bone porosity can be determined with reasonable accuracy. The inversion procedure is based on direct minimization of an objective function involving the pressure field measured at locations near the bone sample.

Keywords: Biot model, boundary integral method, cancellous bone, minimization procedure, ultrasound

(Some figures may appear in colour only in the online journal)

1. Introduction

Osteoporosis is characterized by a decrease in the strength of the bone matrix [15, 16]. This is a serious disease affecting an increasing number of the aged and it is also a threat for potential astronauts. Since only 70% of the variance of bone strength is accounted for by bone density,

quantitative ultrasound techniques could provide a new diagnostic tool for determining more accurately the actual rigidity [19, 20, 34]. In contrast to x-ray densitometry, ultrasound technology does not ionize the tissue and its implementation is relatively inexpensive. However, it is limited to only a few skeletal sites compared to radiographic methods. Since the loss of bone density and the destruction of the bone microstructure is most evident in osteoporotic cancellous bone, which consists of trabeculae and marrow, it is natural to consider the possibility of developing accurate ultrasound models for the sonification of cancellous bone. It would be of enormous clinical advantage if accurate methods could be developed using ultrasonic interrogation to diagnose osteoporosis and bone fractures.

Cancellous bone is a two-component material consisting of a calcified bone matrix with interspinal fatty marrow. Therefore, mathematical models of poro-elastic media may be applicable [2–5, 7, 8, 17, 21, 33, 37, 38, 40]. In particular, McKelvie and Palmer [35], Williams [41] and Hosokawa and Otani [30] discussed the application of Biot's model for a poro-elastic medium to the case of cancellous bone. Use of this model requires determination of the physical parameters upon which it depends. This can be an expensive process. In this article, we investigate whether these parameters can be ascertained by acoustic interrogation.

Earlier work on this inverse problem includes Buchanan *et al*'s [11] who used the finite-element method to solve Biot's equations for a two-dimensional bone specimen immersed in a finite water tank. This numerical approach is rather intensive as it requires discretizing the entire domain. The geometric aspect ratio is such that the region of interest (i.e. the bone specimen) is significantly smaller than the water tank, hence a large portion of the discretization is not used to resolve the bone itself. Finite-size effects in the water tank also pose numerical difficulties as a number of eigenvalues need to be resolved for accurate computation. Partly for this reason, Buchanan *et al* [11] performed acoustic interrogation with relatively low frequencies, in the 5–15 kHz range. This was accomplished by placing an illuminating source in the tank near one side of the bone specimen. They attempted to recover several Biot parameters via direct minimization of an objective function on the pressure field measured at locations on the opposite side to the source. Lacking experimental data, the 'measured' values were artificially generated based on a highly resolved numerical solution of Biot's model. In doing so, their algorithm was most successful at determining the bone porosity, with errors of less than 3%.

Recently, Gilbert *et al* [22, 27] examined the same inverse problem but, in an effort to reduce the computational cost, they adopted a boundary integral approach to solve for the fluid domain. More specifically, the pressure field at any point in the water is given by a boundary integral equation in terms of the Green's function for Helmholtz's equation. However, they considered the idealized situation where the water tank is of infinite extent in all directions. As a result, the Green's function reduces to a simple Hankel's function and the boundary integral equation for the pressure field is simply defined along the boundary of the bone specimen. This implies that only the region occupied by the bone sample needs to be discretized. Besides computational considerations, Gilbert *et al* [27] also implemented a more refined Biot's model featuring a new variable to compensate for the shortage of transmission conditions, together with a more realistic representation of viscous friction due to pore tortuosity, as compared to [11].

If the geometry is further simplified to be one-dimensional, so that the bone sample reduces to a segment and water extends to infinity on both sides, then explicit analytical expressions for the exterior pressure field can be derived. This direction of inquiry was pursued by e.g. Sebaa *et al* [39] and Buchanan *et al* [12] to tackle the inverse problem, yielding good results. Sebaa *et al* [39] used actual measurements from laboratory experiments in their recovery process, while Buchanan *et al* [12] proposed a numerical algorithm to help improve convergence

in the minimization procedure by refining the choice of initial guesses. In addition to this body of work, another major line of investigation seeks to estimate and use wave parameters from ultrasonic echoes as a possible tool for the diagnosis of osteoporosis [1, 29]. A review on inverse problems in elasticity can be found in [6].

In the present paper, we extend the results of Gilbert *et al* [27] to the more physical setting of a finite water tank with an upper free surface. For computational purposes, Helmholtz's equation is again reduced to a boundary integral equation defined along the interface between bone and water. This is made possible by devising a Green's function that satisfies the various conditions imposed at the exterior boundaries of the tank. For a two-dimensional rectangular geometry, this Green's function is explicitly derived via the method of images and is expressed as a double series in terms of Hankel's functions. The resulting boundary value problem is thus nonlocal, and its well-posedness is established via a variational formulation. An asymptotic analysis is also carried out to estimate the convergence rate of the series expansion for the Green's function. Having the parameter recovery problem in mind, a finite-difference scheme is developed to solve the equations numerically. Sensitivity and recovery tests are performed with an emphasis on the bone porosity. Two distinct frequencies in the ultrasonic range are used for the acoustic interrogation (250 and 500 kHz), and parameter recovery is accomplished via error minimization on the pressure field.

The remainder of this paper is organized as follows. Section 2 introduces Biot's model for cancellous bone in the time-harmonic isotropic case. Section 3 describes the nonlocal boundary value problem for a two-dimensional bone sample immersed in a water tank. This includes a discussion on the variational formulation and its well-posedness, as well as a derivation of the Green's function. Section 4 examines the convergence rate of the series expansion for the Green's function, as this is relevant for its numerical approximation. Section 5 presents the finite-difference scheme to solve the boundary value problem numerically. Section 6 discusses the sensitivity and recovery tests based on this numerical model. The minimization procedure for trial values relative to measured values of the pressure field is explained in detail. Both cases of univariate and multivariate minimization are considered in an effort to recover the bone porosity and additional parameters. Finally, concluding remarks are given in section 7.

2. Biot–Johnson model for cancellous bone

The Biot–Johnson model treats a poro-elastic medium as an elastic frame with interspinal pore fluid [3–5, 40]. Cancellous bone is anisotropic; however, as pointed out by Williams [41], if the acoustic waves passing through the bone specimen travel in the trabecular direction, then an isotropic model may be acceptable. We also assume that the medium is homogeneous and accordingly all the parameters are constant throughout the bone specimen. We will simulate a two-dimensional version of the experiments described in [30, 35]. The motions of the frame and fluid within the bone are tracked by position vectors $\mathbf{u} = (u_1, u_2)$ and $\mathbf{U} = (U_1, U_2)$, respectively. In Cartesian coordinates $\mathbf{x} = (x_1, x_2)$, the constitutive equations are those for a linear isotropic elastic material with terms added to account for the interaction between the frame and interstitial fluid,

$$\begin{aligned} \sigma_{11} &= 2\mu e_{11} + \lambda e + Q\varepsilon, \\ \sigma_{22} &= 2\mu e_{22} + \lambda e + Q\varepsilon, \\ \sigma_{12} &= \mu e_{12}, \\ \sigma_{21} &= \mu e_{21}, \end{aligned} \tag{1}$$

where the solid and fluid dilatations are given by

Table 1. Parameters in the Biot–Johnson model for cancellous bone.

Symbol	Parameter	Units
ρ_f	Density of pore fluid	kg m^{-3}
ρ_r	Density of frame material	kg m^{-3}
K_b	Complex frame bulk modulus	Pa
μ	Complex frame shear modulus	Pa
K_f	Fluid bulk modulus	Pa
K_r	Frame material bulk modulus	Pa
k	Permeability	m^2
a	Pore size	m
η	Viscosity of pore fluid	kg m^{-1} s^{-1}
Λ	Viscous characteristic length	m
ω	Frequency	s^{-1}
β	Porosity	
α_∞	Asymptotic tortuosity	

$$e = \nabla \cdot \mathbf{u} = \frac{\partial u_1}{\partial x_1} + \frac{\partial u_2}{\partial x_2}, \quad \varepsilon = \nabla \cdot \mathbf{U} = \frac{\partial U_1}{\partial x_1} + \frac{\partial U_2}{\partial x_2}, \tag{2}$$

respectively. The strains are defined by

$$e_{11} = \frac{\partial u_1}{\partial x_1}, \quad e_{12} = e_{21} = \frac{1}{2}\left(\frac{\partial u_1}{\partial x_2} + \frac{\partial u_2}{\partial x_1}\right), \quad e_{22} = \frac{\partial u_2}{\partial x_2}. \tag{3}$$

The complex frame shear modulus μ is a measured quantity. The other parameters λ, Q and R in the constitutive equations are calculated from the measured or estimated values of the parameters given in table 1 using the Biot–Stoll formulas

$$\begin{aligned} \lambda &= K_b - \frac{2}{3}\mu + \frac{(K_r - K_b)^2 - 2\beta K_r(K_r - K_b) + \beta^2 K_r^2}{D - K_b}, \\ Q &= \frac{\beta K_r\big[(1-\beta)K_r - K_b\big]}{D - K_b}, \\ R &= \frac{\beta^2 K_r^2}{D - K_b}, \end{aligned} \tag{4}$$

where

$$D = K_r\left[1 + \beta\left(\frac{K_r}{K_f} - 1\right)\right].$$

The bulk and shear moduli K_b and μ are often given imaginary parts to account for viscoelasticity. As a reference, the porosity takes the limiting value $\beta = 0$ if cancellous bone is purely solid and $\beta = 1$ if it is purely fluid.

Assuming that the bone system oscillates harmonically, i.e.

$$\mathbf{u}(x_1, x_2, t) = \widehat{\mathbf{u}}(x_1, x_2)\, \mathrm{e}^{\mathrm{i}\omega t}, \quad \mathbf{U}(x_1, x_2, t) = \widehat{\mathbf{U}}(x_1, x_2)\, \mathrm{e}^{\mathrm{i}\omega t},$$

and using an improvement over the Biot–Stoll model, as proposed by Johnson *et al* [32] to replace the Biot assumption of circular/cylindrical pores by a more accurate dissipation term allowing for pore tortuosity, we arrive at the equations

$$\mu\,\nabla^2\mathbf{u} + \nabla\Big[(\lambda+\mu)\,e + Q\,\varepsilon\Big] + p_{11}\,\mathbf{u} + p_{12}\,\mathbf{U} = \mathbf{0},$$
$$\nabla(Q\,e + R\,\varepsilon) + p_{12}\,\mathbf{u} + p_{22}\,\mathbf{U} = \mathbf{0}, \tag{5}$$

where

$$p_{11} = \omega^2\Big[(1-\beta)\rho_r + \beta\rho_f\big(\alpha(\omega)-1\big)\Big],$$
$$p_{12} = -\omega^2\beta\rho_f\big(\alpha(\omega)-1\big),$$
$$p_{22} = \omega^2\beta\rho_f\alpha(\omega),$$

and

$$\alpha(\omega) = \alpha_\infty\left(1 + \frac{\mathrm{i}\eta\beta}{\omega\alpha_\infty\rho_f k}\sqrt{1 + \frac{4\alpha_\infty^2 k^2\rho_f\omega}{\mathrm{i}\eta\Lambda^2\beta^2}}\right).$$

For convenience, we have dropped the hats from $\widehat{\mathbf{u}}$ and $\widehat{\mathbf{U}}$ in (5). The permeability is given by the Kozeny–Carman formula

$$k = \frac{\beta a^2}{4K},$$

where $K = 5$ is an empirical constant. The pore size a is approximately a linear function of porosity [11].

3. Boundary value problem

Under consideration is the typical setup of an *in vitro* experiment [30, 35]. A bone specimen is placed in an open rectangular water tank of width W and height H. The regions occupied by the bone specimen and the water are denoted by Ω^b and Ω^w, respectively (figure 1). In Ω^w, the fluid pressure P and fluid displacement $\mathbf{U}^w = (U_1^w, U_2^w)$ satisfy

$$-\nabla^2 P - \kappa_0^2 P = f, \tag{6}$$

$$\nabla P - \rho^w\omega^2\mathbf{U}^w = \mathbf{0}, \quad \mathbf{x} \neq \mathbf{x}_0, \tag{7}$$

where ρ^w is the water density, $f(\mathbf{x},\mathbf{x}_0) = -q\,\delta(\mathbf{x},\mathbf{x}_0;\kappa_0)$ represents a point source of strength q located at $\mathbf{x} = \mathbf{x}_0$, and κ_0 is the wavenumber of the emitted signal. Reflecting boundary conditions for the pressure are specified on the sides and base of the tank. On the top free surface, a pressure release condition is imposed. Using the method of images, it is possible to construct the Green's function for the pressure in a tank that does not contain any submerged object. We shall use this Green's function in a boundary integral method to calculate the solution for a bone sample immersed in the tank. We next indicate how to calculate the Green's function.

3.1. Green's function for the tank

We assume there is a positive source at $\mathbf{x}_0 = (x_0, y_0) \in \Omega^w$. In order to have reflecting lateral boundaries at $x_1 = 0$ and $x_1 = W$, we place a positive source at $(-x_0, y_0)$ and another at $(2W - x_0, y_0)$. However, the source at $(-x_0, y_0)$ changes the reflection at $x_1 = W$ and the source at $(2W - x_0, y_0)$ changes the reflection at $x_1 = 0$. This leads us to using reflection to place positive sources at $(-2W + x_0, y_0)$ and $(2W + x_0, y_0)$. Proceeding in this manner to

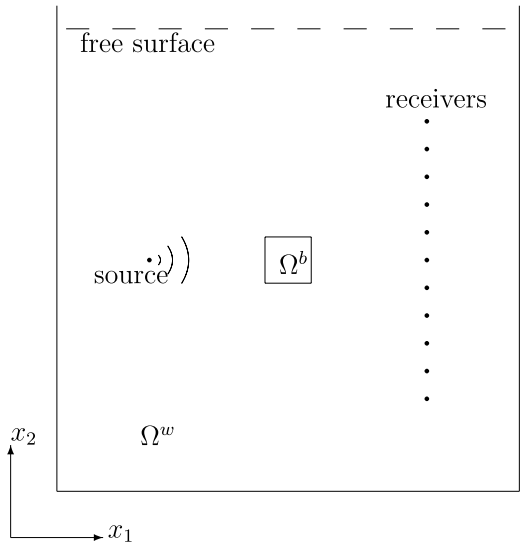

Figure 1. Sketch of the experimental setup for the acoustic interrogation of a bone specimen Ω^b in a water tank Ω^w.

correct the non-reflecting property posed by adding another source leads to positive sources being placed at the infinite sequence of points

$$(2\ell W - x_0, y_0) \quad \text{and} \quad (2\ell W + x_0, y_0), \quad \ell = 0, \pm 1, \pm 2, \ldots.$$

These charges will effect the potentials on the upper layer and the bottom of the tank, and we will have to add further charges to counterbalance these; i.e. each reflected charge changes the potentials on the horizontal surfaces, which in turn require extra charges to keep these surfaces as reflecting boundaries. In order to have a zero boundary condition at $x_2 = H$, we place a negative charge at $(x_0, 2H + y_0)$. To retain the reflecting bottom boundary, a positive charge is placed at $(x_0, -y_0)$. This procedure is continued by changing the charge sign each time we reflect through $x_2 = H$ while maintaining the same charge when we reflect through $x_2 = 0$. This leads to placing charges at the points

$$(x_0, 2mH - y_0) \quad \text{and} \quad (x_0, 2mH + y_0), \quad m = 0, \pm 1, \pm 2, \ldots.$$

On the other hand, the charge associated with reflections through the pressure release surface follows a different rule: if $m/2$ is an integer, the charge is to be positive otherwise it is negative. These sources also disturb the potentials on the vertical sides and we have to make a correction for this. Hence each correctional source we made to the vertical sides will need to be reflected in the x_2-direction, and each correctional source we added to maintain the reflecting bottom and pressure release surface must be reflected in the horizontal x_1-direction. The way we construct our Green's function is similar to that described in [14] although we deal with Helmholtz's equation rather than Laplace's equation, and the boundary conditions are different. The reflection method also works for Helmholtz's equation because it is translation-invariant. In arranging these source points, we arrive at the array

$$(x_0 + 2\ell W, -y_0 + 2mH), \quad (-x_0 + 2\ell W, -y_0 + 2mH),$$

$$(x_0 + 2\ell W, y_0 + 2mH), \quad (-x_0 + 2\ell W, y_0 + 2mH), \quad \ell, m = 0, \pm 1, \pm 2, \ldots.$$

This permits us to find an infinite series representation of the Green's function for Helmholtz's equation in an open water tank,

$$\begin{aligned} G(\mathbf{x},\mathbf{x}_0;\kappa_0) = \mathrm{i}\pi \sum_{\ell=-\infty}^{\infty}\sum_{m=-\infty}^{\infty} (-1)^m \Big[& H_0^{(1)}\Big(\kappa_0\sqrt{(x_1-x_0-2\ell W)^2+(x_2+y_0-2mH)^2}\Big) \\ & + H_0^{(1)}\Big(\kappa_0\sqrt{(x_1+x_0-2\ell W)^2+(x_2+y_0-2mH)^2}\Big) \\ & + H_0^{(1)}\Big(\kappa_0\sqrt{(x_1-x_0-2\ell W)^2+(x_2-y_0-2mH)^2}\Big) \\ & + H_0^{(1)}\Big(\kappa_0\sqrt{(x_1+x_0-2\ell W)^2+(x_2-y_0-2mH)^2}\Big)\Big], \end{aligned} \tag{8}$$

where $H_0^{(1)}(z)$ denotes the Hankel's function of the first kind [18].

3.2. Modified Biot equations for the bone

In order to formulate a well-posed boundary value problem, we must modify the Biot equation (5) since there are not enough transmission conditions for the components of displacements fields u_1, u_2, U_1 and U_2. The main idea here is to replace the unknowns U_1 and U_2 by the single variable $s = Q\,e + R\,\varepsilon$ in the equations. To accomplish this, we first express ε and $\mathbf{U}$ in terms of s from (1) and (5),

$$\varepsilon = \frac{1}{R}(s - Q\,e), \quad \mathbf{U} = -\frac{1}{p_{22}}(\nabla s + p_{12}\,\mathbf{u}). \tag{9}$$

Then, by taking the divergence of the second equation in (5), we obtain

$$\nabla^2 s + p_{12}\,e + p_{22}\,\varepsilon = 0,$$

which reduces to

$$\nabla^2 s + \frac{p_{22}}{R}s + \left(p_{12} - \frac{p_{22}Q}{R}\right)e = 0, \tag{10}$$

after using (9). Similarly, the first equation of (5) can be written in the form

$$\mu\,\nabla^2\mathbf{u} + \nabla\left[\left(\lambda+\mu-\frac{Q^2}{R}\right)e + \left(\frac{Q}{R}-\frac{p_{12}}{p_{22}}\right)s\right] + \left(p_{11}-\frac{p_{12}^2}{p_{22}}\right)\mathbf{u} = \mathbf{0}. \tag{11}$$

3.3. Transmission conditions

Equations (10) and (11) represent the modified Biot equations for $\mathbf{u}$ and s in the bone specimen Ω^b. These equations should be satisfied by $\mathbf{u}$ and s together with transmission conditions at the interface between bone and water. These are:

- Continuity of the aggregate pressure:

$$\sigma_{\ell j}\,n_j + s\,n_\ell = -P\,n_\ell, \tag{12}$$

since an expansion of the bone induces a compression in the water. Here $\sigma_{\ell j}$ denotes the components of the stress tensor as defined in (1) and n_ℓ denotes the components of the exterior unit normal $\mathbf{n}$ to Ω^b (which points into the water).

- Continuity of the flux: from (7), we have

$$\rho^w\omega^2\Big[\beta\,\mathbf{n}\cdot\mathbf{U}+(1-\beta)\,\mathbf{n}\cdot\mathbf{u}\Big]=\rho^w\omega^2\,\mathbf{n}\cdot\mathbf{U}^w,$$

  and thus

$$\rho^w\omega^2\left(\left[1-\beta\left(1+\frac{p_{12}}{p_{22}}\right)\right]\mathbf{n}\cdot\mathbf{u}-\frac{\beta}{p_{22}}\frac{\partial s}{\partial n}\right)=\frac{\partial P}{\partial n}. \tag{13}$$

- Continuity of the pore pressure:

$$s=-\beta\,P. \tag{14}$$

- Vanishing of the tangential frame stress: $\sigma_{12}\equiv\sigma_{21}=0$ which is equivalent to

$$\frac{\partial u_1}{\partial x_2}+\frac{\partial u_2}{\partial x_1}=0. \tag{15}$$

We have so far given the precise formulation of the bounded transmission problem (BTP) consisting of the bulk equations (10) and (11) for the unknowns $\mathbf{u}$ and s in Ω^b as well as the bulk equation (6) for the unknown P in Ω^w together with the transmission conditions (12)–(15).

From a computational point of view, it is more convenient to reduce this BTP to a nonlocal problem posed in a small domain such as Ω^b. By doing so, unlike [11], we avoid having to discretize the entire water tank, which thus saves in memory and CPU time. For this purpose, we reduce Helmholtz's equation (6) to a boundary integral equation via the Green's representation of P in Ω^w. More precisely, we seek a solution of (6) in the form of a single-layer potential for the unknown density function φ,

$$P(\mathbf{x},\mathbf{x}_0)=P_f(\mathbf{x},\mathbf{x}_0)-\int_{\partial\Omega^b}G(\mathbf{x},\zeta;\kappa_0)\varphi(\mathbf{x}_0,\zeta)\,\mathbf{d}S_\zeta,\quad \mathbf{x}\in\Omega^w, \tag{16}$$

where

$$P_f(\mathbf{x},\mathbf{x}_0)=\int_{\mathrm{supp}(f)}G(\mathbf{x},\mathbf{y};\kappa_0)f(\mathbf{y},\mathbf{x}_0)\,\mathrm{d}\mathbf{y}=-q\,G(\mathbf{x},\mathbf{x}_0;\kappa_0),$$

and $G(\mathbf{x},\mathbf{x}_0;\kappa_0)$ is given by (8). Clearly, the unknown density function φ is related to the unknowns $\mathbf{u}$ and $\mathbf{U}$ via the transmission conditions (12)–(15).

If the bone boundary $\partial\Omega^b$ has positive orientation, then letting $\mathbf{x}\to\mathbf{X}\in\partial\Omega^b$, we obtain from (12) that

$$\lambda\,\nabla\cdot\mathbf{u}+2\mu\frac{\partial u_1}{\partial x_1}+Q\,\varepsilon+s=q\,G(\mathbf{X},\mathbf{x}_0;\kappa_0)+\int_{\partial\Omega^b}G(\mathbf{X},\zeta;\kappa_0)\varphi(\mathbf{x}_0,\zeta)\,\mathbf{d}S_\zeta, \tag{17}$$

and

$$\lambda\,\nabla\cdot\mathbf{u}+2\mu\frac{\partial u_2}{\partial x_2}+Q\,\varepsilon+s=q\,G(\mathbf{X},\mathbf{x}_0;\kappa_0)+\int_{\partial\Omega^b}G(\mathbf{X},\zeta;\kappa_0)\varphi(\mathbf{x}_0,\zeta)\,\mathbf{d}S_\zeta, \tag{18}$$

where ε is given by (9). Note that, in deriving these equations, we have tacitly employed (15). In view of the similarity between (17) and (18), a subtraction of these two equations leads to the simple relation

$$\frac{\partial u_1}{\partial x_1}-\frac{\partial u_2}{\partial x_2}=0. \tag{19}$$

Hence, in numerical computation, we may use (19) and either (17) or (18), but not both.

Next, the flux continuity condition (13) leads to a natural boundary condition for s,

$$\begin{aligned}&\rho^w\omega^2\left(\left[1-\beta\left(1+\frac{p_{12}}{p_{22}}\right)\right]\mathbf{n}\cdot\mathbf{u}-\frac{\beta}{p_{22}}\frac{\partial s}{\partial n}\right)+q\frac{\partial G}{\partial n}(\mathbf{X},\mathbf{x}_0;\kappa_0)\\&=\frac{1}{2}\varphi(\mathbf{x}_0,\mathbf{X})-\int_{\partial\Omega^b}\varphi(\mathbf{x}_0,\zeta)\frac{\partial G}{\partial n}(\mathbf{X},\zeta;\kappa_0)\,\mathbf{d}S_\zeta.\end{aligned}\tag{20}$$

Finally, from the representation formula for P, applying the trace operator on $\partial\Omega^b$ to (16) and using (14) leads to a boundary integral equation for φ,

$$\beta\,\mathbf{V}\varphi-s+\beta\,\gamma_0\,q\,G(\mathbf{X},\mathbf{x}_0;\kappa_0)=0,\tag{21}$$

where

$$\mathbf{V}\varphi=\gamma_0\int_{\partial\Omega^b}G(\mathbf{X},\zeta;\kappa_0)\varphi(\mathbf{x}_0,\zeta)\,\mathbf{d}S_\zeta,$$

and γ_0 is the trace operator from $H^1(\Omega^b)$ to $L^2(\partial\Omega^b)$. The right-hand sides of (17) and (18) and left-hand sides of (20) and (21) contain no singularity, since the source point $\mathbf{x}_0$ is in Ω^w.

3.4. Well-posedness of the variational formulation

Before we formulate what is called the nonlocal problem for this BTP, some observations are in order. We observe that the transmission conditions (17) and (18) can be considered as natural boundary conditions for the displacement field $\mathbf{u}$ given s and φ, whereas condition (20) is a natural condition for the stress s, if $\mathbf{u}$ and φ are known. From a variational point of view, both equations define the relevant Dirichlet-to-Neumann maps. On the other hand, condition (21) only relates the trace of the stress s and the known density function φ, which may be considered as a boundary integral equation for φ given the stress s.

By construction of the Green's function, the fluid pressure is here expressed in terms of a boundary integral equation defined on $\partial\Omega^b$ alone, which is similar to the case of an infinite water tank as treated in [22, 27, 28]. By mirroring the arguments of Gilbert *et al* [28], we can define the nonlocal problem, propose a variational formulation and show its well-posedness. For convenience, we only outline the main steps in this analysis and refer the reader to [28] for more details.

Definition 1 (Nonlocal boundary value problem). The transmission problem TP_f is termed a nonlocal boundary value problem for the triplet $(\mathbf{u}, s, \varphi)$ if the latter satisfies the bulk equations (10) and (11) and the boundary integral equation (16) together with the transmission conditions

$$\left(\underline{\underline{\sigma}}(\mathbf{u})+Q\,\nabla\cdot\mathbf{U}+s\right)\mathbf{n}=-P\,\mathbf{n},\quad\text{on}\quad\partial\Omega^b,\tag{22}$$

and

$$\rho^w\omega^2\left(\left[1-\beta\left(1+\frac{p_{12}}{p_{22}}\right)\right]\mathbf{u}\cdot\mathbf{n}-\frac{\beta}{p_{22}}\frac{\partial s}{\partial n}\right)=\frac{\partial P}{\partial n},\quad\text{on}\quad\partial\Omega^b,\tag{23}$$

where

$$P=-\mathbf{V}\varphi+\gamma_0 P_f,\quad\frac{\partial P}{\partial n}=\frac{1}{2}\varphi-\mathbf{K}'\varphi+\frac{\partial P_f}{\partial n}.$$

The boundary integral operator $\mathbf{K}'$ is defined by

$$\begin{aligned}\mathbf{K}'\varphi(\mathbf{x}_0,\mathbf{X}) &= \langle\varphi, \frac{\partial G}{\partial n}\rangle_{\partial\Omega^b},\\ &= \int_{\partial\Omega^b}\varphi(\mathbf{x}_0,\zeta)\frac{\partial G}{\partial n}(\mathbf{X},\zeta;\kappa_0)\,\mathbf{d}S_\zeta, \quad \mathbf{X}\in\partial\Omega^b,\end{aligned}$$

and

$$\underline{\underline{\sigma}}(\mathbf{u}) = \lambda\nabla\cdot\mathbf{u} + 2\mu\,\underline{\underline{e}}(\mathbf{u}), \quad \underline{\underline{e}}(\mathbf{u}) = \frac{1}{2}\big(\nabla\mathbf{u}+\nabla\mathbf{u}^\top\big),$$

represent the stress and strain tensors, respectively. We note that condition (23) can be explicitly written in terms of φ as

$$\frac{\partial s}{\partial n} = \frac{p_{22}}{\beta}\left\{\left[1-\beta\left(1+\frac{p_{12}}{p_{22}}\right)\right]\mathbf{u}\cdot\mathbf{n} - \frac{1}{\rho^w\omega^2}\left(\frac{1}{2}\varphi - \mathbf{K}'\varphi\right)\right\} - \frac{p_{22}}{\beta\rho^w\omega^2}\frac{\partial P_f}{\partial n}.$$

Definition 2 (Traction-free problem). The traction-free problem consists in finding the pair $(\mathbf{u}, s)$ that satisfies the bulk equations (10) and (11) in Ω^b, together with the homogeneous boundary conditions

$$\big(\underline{\underline{\sigma}}(\mathbf{u}) + Q\nabla\cdot\mathbf{U} + s\big)\,\mathbf{n} = \mathbf{0}, \quad \text{on} \quad \partial\Omega^b,$$

$$\rho^w\omega^2\left(\left[1-\beta\left(1+\frac{p_{12}}{p_{22}}\right)\right]\mathbf{u}\cdot\mathbf{n} - \frac{\beta}{p_{22}}\frac{\partial s}{\partial n}\right) = 0, \quad \text{on} \quad \partial\Omega^b,$$

$$s = 0, \quad \text{on} \quad \partial\Omega^b.$$

The corresponding nontrivial solutions are referred to as the traction-free solutions.

Definition 3 (Variational formulation). Find the triplet

$$(\mathbf{u}, s, \varphi) \in \big(H^1(\Omega^b)\big)^2 \times H^1(\Omega^b) \times H^{-1/2}(\partial\Omega^b),$$

such that

$$\mathcal{A}\Big\{(\mathbf{u}, s, \varphi), (\mathbf{v}, \tau, \psi)\Big\} = \mathcal{L}_f(\mathbf{v}, \tau, \psi), \tag{24}$$

for all

$$(\mathbf{v}, \tau, \psi) \in \big(H^1(\Omega^b)\big)^2 \times H^1(\Omega^b) \times H^{-1/2}(\partial\Omega^b),$$

where $\mathcal{A}$ and $\mathcal{L}_f$ are respectively the sesquilinear form and linear functional defined by

$$\begin{aligned}\mathcal{A}\Big\{(\mathbf{u}, s, \varphi), (\mathbf{v}, \tau, \psi)\Big\} &= a(\mathbf{u},\mathbf{v}) + b(s,\tau) + \frac{p_{22}}{2\rho^w\omega^2}\langle\mathbf{V}\varphi, \overline{\psi}\rangle_{\partial\Omega^b}\\ &+ \left(\frac{Q}{R} - \frac{p_{12}}{p_{22}}\right)\left(\int_{\Omega^b} s\,\nabla\cdot\overline{\mathbf{v}}\,\mathrm{d}\mathbf{x} + p_{22}\int_{\Omega^b}(\nabla\cdot\mathbf{u})\,\overline{\tau}\,d\mathbf{x}\right)\\ &- \left(p_{11} - \frac{p_{12}^2}{p_{22}}\right)\int_{\Omega^b}\mathbf{u}\cdot\overline{\mathbf{v}}\,\mathrm{d}\mathbf{x} - \frac{p_{22}}{R}\int_{\Omega^b} s\,\overline{\tau}\,\mathrm{d}\mathbf{x}\\ &- \left[1-\beta\left(1+\frac{p_{12}}{p_{22}}\right)\right]\left(\langle\mathbf{V}\varphi\,\mathbf{n}, \overline{\mathbf{v}}\rangle_{\partial\Omega^b} + \frac{p_{22}}{\beta}\langle\mathbf{u}\cdot\mathbf{n}, \overline{\tau}\rangle_{\partial\Omega^b}\right)\\ &+ \frac{p_{22}}{\beta\rho^w\omega^2}\left(\langle\frac{1}{2}\varphi - \mathbf{K}'\varphi, \overline{\tau}\rangle_{\partial\Omega^b} - \frac{1}{2}\langle s, \overline{\psi}\rangle_{\partial\Omega^b}\right),\end{aligned} \tag{25}$$

and

$$\mathcal{L}_f(\mathbf{v},\tau,\psi) = -\left[1-\beta\left(1+\frac{p_{12}}{p_{22}}\right)\right]\langle\gamma_0 P_f\,\mathbf{n},\overline{\mathbf{v}}\rangle_{\partial\Omega^b} - \frac{p_{22}}{\beta\rho^w\omega^2}\langle\frac{\partial P_f}{\partial n},\overline{\tau}\rangle_{\partial\Omega^b} + \frac{p_{22}}{2\rho^w\omega^2}\langle\gamma_0 P_f,\overline{\psi}\rangle_{\partial\Omega^b}. \tag{26}$$

In the above, the sesquilinear forms $a(\mathbf{u},\mathbf{v})$ and $b(s,\tau)$ are defined as

$$a(\mathbf{u},\mathbf{v}) = \int_{\Omega^b}\left[\left(\lambda-\frac{Q^2}{R}\right)(\nabla\cdot\mathbf{u})(\nabla\cdot\overline{\mathbf{v}}) + 2\mu\,\underline{\underline{e}}(\mathbf{u}):\underline{\underline{e}}(\overline{\mathbf{v}})\right]\mathrm{d}\mathbf{x}, \tag{27}$$

and

$$b(s,\tau) = \int_{\Omega^b}\nabla s\cdot\nabla\overline{\tau}\,\mathrm{d}\mathbf{x}. \tag{28}$$

The variational equation (24) is obtained after multiplying (10), (11) and (21) by the conjugates of τ, $\mathbf{v}$, ψ respectively, then integrating by parts over their domains of definition and finally combining their expressions. The triplet $(\mathbf{v},\tau,\psi)$ represents test functions in this variational formulation.

From the definition (25) of $\mathcal{A}$, it follows that

$$\mathrm{Re}\mathcal{A}\Big\{(\mathbf{u},s,\varphi),(\mathbf{u},s,\varphi)\Big\} = a(\mathbf{u},\mathbf{u}) + b(s,s) + \frac{p_{22}}{2\rho^w\omega^2}\langle\mathbf{V}\varphi,\overline{\varphi}\rangle_{\partial\Omega^b} + \mathcal{C}\Big\{(\mathbf{u},s,\varphi),(\mathbf{u},s,\varphi)\Big\},$$

where $\mathcal{C}$ is compact on $\left(H^1(\Omega^b)\right)^2\times H^1(\Omega^b)\times H^{-1/2}(\partial\Omega^b)$. Consequently, it is not difficult to prove the following result.

Theorem 1. *The sesquilinear form $\mathcal{A}$ satisfies Gårding's inequality in the form*

$$\mathrm{Re}\mathcal{A}\Big\{(\mathbf{u},s,\varphi),(\mathbf{u},s,\varphi)\Big\} \geqslant \alpha\left(\|\mathbf{u}\|^2_{(H^1(\Omega^b))^2} + \|s\|^2_{H^1(\Omega^b)} + \|s\|^2_{H^{-\frac{1}{2}}(\partial\Omega^b)}\right) - \delta\left(\|\mathbf{u}\|^2_{(H^{1-\epsilon}(\Omega^b))^2} + \|s\|^2_{H^{1-\epsilon}(\Omega^b)} + \|s\|^2_{H^{-\frac{1}{2}-\epsilon}(\partial\Omega^b)}\right),$$

where $\alpha>0$ and $\delta\geqslant 0$ are constants, and $\epsilon>0$ is a small parameter.

As is well known, Gårding's inequality implies the validity of Fredholm's alternative. Hence, uniqueness implies existence. For this purpose, we now consider the homogeneous transmission problem TP_f with $f=0$, since uniqueness of the solution to the variational equation (24) depends upon that of TP_f.

Theorem 2. *If the triplet $(\mathbf{u},s,P)$ is a classical solution of the homogeneous transmission problem TP_0 with $\mathrm{Im}\kappa_0=0$, then $P=0$.*

The proof follows the standard uniqueness approach for the scattering transmission problem [28]. Theorem 2 does not imply that components $(\mathbf{u},s)$ of the triplet $(\mathbf{u},s,P)$ in the TP_0 are trivial solutions, since they may be solutions of the traction-free problem. In order to ensure the existence of a solution to the variational equation (24), we make the following assumptions.

(i) There is no traction-free solution.
(ii) The square κ_0^2 of the wavenumber is not an eigenvalue of the Dirichlet problem for the negative Laplacian in Ω^b.

Assumption 2 is a guarantee for invertibility of the single-layer operator $\mathbf{V}$ [31]. The last theorem summarizes these results.

Theorem 3. *Under assumptions 1 and 2, there exists a unique solution of the TP$_f$ in* $\left(H^1(\Omega^b)\right)^2 \times H^1(\Omega^b) \times H^{-1/2}(\partial\Omega^b)$.

4. Approximating the Green's function

In practice, the series representation of the Green's function is approximated by a finite number of terms and so to decide how many of them should be included, we need to consider asymptotic approximations of the Hankel's functions appearing in the higher-order reflective sources. The Green's function is given here by a double series, which reflects the two-dimensional geometry of the problem, but the horizontal and vertical directions are not equivalent since they correspond to different boundary conditions in the tank. Accordingly, we will examine different cases depending on the index of summation ℓ or m.

To this end, we introduce the notation

$$\mathbf{x}_{\ell m}^{(1)} = (x_0 + 2\ell W, -y_0 + 2mH), \quad \mathbf{x}_{\ell m}^{(2)} = (-x_0 + 2\ell W, -y_0 + 2mH),$$

$$\mathbf{x}_{\ell m}^{(3)} = (x_0 + 2\ell W, y_0 + 2mH), \quad \mathbf{x}_{\ell m}^{(4)} = (-x_0 + 2\ell W, y_0 + 2mH),$$

and rewrite the Green's function as

$$G(\mathbf{x}, \mathbf{x}_0; \kappa_0) = \mathrm{i}\pi \sum_{\ell=-\infty}^{\infty} \sum_{m=-\infty}^{\infty} (-1)^m \Big[H_0^{(1)}\left(\kappa_0 \|\mathbf{x} - \mathbf{x}_{\ell m}^{(1)}\|\right) + H_0^{(1)}\left(\kappa_0 \|\mathbf{x} - \mathbf{x}_{\ell m}^{(2)}\|\right) + H_0^{(1)}\left(\kappa_0 \|\mathbf{x} - \mathbf{x}_{\ell m}^{(3)}\|\right) + H_0^{(1)}\left(\kappa_0 \|\mathbf{x} - \mathbf{x}_{\ell m}^{(4)}\|\right) \Big].$$

As $|\ell|, |m| \to \infty$, we have the estimates

$$\|\mathbf{x} - \mathbf{x}_{\ell m}^{(1)}\| \to 2\sqrt{m^2H^2 + \ell^2W^2} \left[1 - \frac{1}{2}\left(\frac{(x_1 - x_0)\ell W + (x_2 + y_0)mH}{m^2H^2 + \ell^2W^2}\right)\right],$$

$$\|\mathbf{x} - \mathbf{x}_{\ell m}^{(2)}\| \to 2\sqrt{m^2H^2 + \ell^2W^2} \left[1 - \frac{1}{2}\left(\frac{(x_1 + x_0)\ell W + (x_2 + y_0)mH}{m^2H^2 + \ell^2W^2}\right)\right],$$

$$\|\mathbf{x} - \mathbf{x}_{\ell m}^{(3)}\| \to 2\sqrt{m^2H^2 + \ell^2W^2} \left[1 - \frac{1}{2}\left(\frac{(x_1 - x_0)\ell W + (x_2 - y_0)mH}{m^2H^2 + \ell^2W^2}\right)\right],$$

$$\|\mathbf{x} - \mathbf{x}_{\ell m}^{(4)}\| \to 2\sqrt{m^2H^2 + \ell^2W^2} \left[1 - \frac{1}{2}\left(\frac{(x_1 + x_0)\ell W + (x_2 - y_0)mH}{m^2H^2 + \ell^2W^2}\right)\right],$$

provided $4\ell^2W + 4m^2H \gg (x_1 - x_0)^2 + (x_2 - y_0)^2$. Now following Morse and Feshbach [36], we approximate the Hankel's functions by

$$H_0^{(1)}\left(\kappa_0\|\mathbf{x}-\mathbf{x}_{\ell m}^{(1)}\|\right)+H_0^{(1)}\left(\kappa_0\|\mathbf{x}-\mathbf{x}_{\ell m}^{(3)}\|\right)$$
$$\simeq \frac{2}{\sqrt{\mathrm{i}\pi\kappa_0\sqrt{m^2H^2+\ell^2W^2}}}\mathrm{e}^{-\mathrm{i}\kappa_0\frac{x_1\ell W+x_2mH}{\sqrt{m^2H^2+\ell^2W^2}}}\cos\left[\frac{\kappa_0(x_0\ell W-y_0mH)}{\sqrt{m^2H^2+\ell^2W^2}}\right],$$

$$H_0^{(1)}\left(\kappa_0\|\mathbf{x}-\mathbf{x}_{\ell m}^{(2)}\|\right)+H_0^{(1)}\left(\kappa_0\|\mathbf{x}-\mathbf{x}_{\ell m}^{(4)}\|\right)$$
$$\simeq \frac{2}{\sqrt{\mathrm{i}\pi\kappa_0\sqrt{m^2H^2+\ell^2W^2}}}\mathrm{e}^{-\mathrm{i}\kappa_0\frac{x_1\ell W+x_2mH}{\sqrt{m^2H^2+\ell^2W^2}}}\cos\left[\frac{\kappa_0(x_0\ell W+y_0mH)}{\sqrt{m^2H^2+\ell^2W^2}}\right].$$

Using such estimates gives precise information on the accuracy of the Green's function approximation.

Simpler estimates are available when $|\ell|\geqslant L$, $|m|\leqslant M$ and when $|\ell|\leqslant L$, $|m|\geqslant M$ for some large integers L and M. Accordingly, we distinguish the various cases

$$\|\mathbf{x}-\mathbf{x}_{\ell m}^{(1)}\|\simeq\begin{cases}2|m|H-(x_2+y_0) & \text{for } |m|\gg 1,|\ell|\leqslant L,\\ 2|\ell|W-(x_1-x_0) & \text{for } |\ell|\gg 1,|m|\leqslant M,\end{cases}$$

$$\|\mathbf{x}-\mathbf{x}_{\ell m}^{(2)}\|\simeq\begin{cases}2|m|H-(x_2+y_0) & \text{for } |m|\gg 1,|\ell|\leqslant L,\\ 2|\ell|W-(x_1+x_0) & \text{for } |\ell|\gg 1,|m|\leqslant M,\end{cases}$$

$$\|\mathbf{x}-\mathbf{x}_{\ell m}^{(3)}\|\simeq\begin{cases}2|m|H-(x_2-y_0) & \text{for } |m|\gg 1,|\ell|\leqslant L,\\ 2|\ell|W-(x_1+x_0) & \text{for } |\ell|\gg 1,|m|\leqslant M,\end{cases}$$

$$\|\mathbf{x}-\mathbf{x}_{\ell m}^{(4)}\|\simeq\begin{cases}2|m|H-(x_2-y_0) & \text{for } |m|\gg 1,|\ell|\leqslant L,\\ 2|\ell|W-(x_1-x_0) & \text{for } |\ell|\gg 1,|m|\leqslant M.\end{cases}$$

This leads to the approximation

$$H_0^{(1)}\left(\kappa_0\|\mathbf{x}-\mathbf{x}_{\ell m}^{(1)}\|\right)+H_0^{(1)}\left(\kappa_0\|\mathbf{x}-\mathbf{x}_{\ell m}^{(3)}\|\right)$$
$$\simeq\sqrt{\frac{1}{\mathrm{i}\pi\kappa_0|m|H}}\left[\mathrm{e}^{\mathrm{i}\kappa_0(2|m|H-(x_2+y_0))}+\mathrm{e}^{\mathrm{i}\kappa_0(2|m|H-(x_2-y_0))}\right],\quad |m|\gg 1.$$

Hence the sum of the remaining terms in the segments $|\ell|\leqslant L, |m|\geqslant M$ is given by

$$R_m^{13}\simeq\frac{2}{\sqrt{\mathrm{i}\pi\kappa_0 H}}\cos(\kappa_0y_0)\,\mathrm{e}^{-\mathrm{i}\kappa_0x_2}\sum_{|m|=M}^{\infty}\frac{\mathrm{e}^{2\mathrm{i}\kappa_0|m|H}}{\sqrt{|m|}},\quad |m|\gg 1,$$

and similarly

$$H_0^{(1)}\left(\kappa_0\|\mathbf{x}-\mathbf{x}_{\ell m}^{(1)}\|\right)+H_0^{(1)}\left(\kappa_0\|\mathbf{x}-\mathbf{x}_{\ell m}^{(3)}\|\right)$$
$$\simeq\sqrt{\frac{1}{\mathrm{i}\pi\kappa_0|\ell|W}}\left[\mathrm{e}^{\mathrm{i}\kappa_0(2|\ell|W-(x_1-x_0))}+\mathrm{e}^{\mathrm{i}\kappa_0(2|\ell|W-(x_1+x_0))}\right],\quad |\ell|\gg 1,$$

with the sum of the remaining terms in the segments $|\ell|\geqslant L, |m|\leqslant M$ being given by

$$R_\ell^{13}\simeq\frac{2}{\sqrt{\mathrm{i}\pi\kappa_0 W}}\cos(\kappa_0x_0)\,\mathrm{e}^{-\mathrm{i}\kappa_0x_1}\sum_{|\ell|=L}^{\infty}\frac{\mathrm{e}^{2\mathrm{i}\kappa_0|\ell|W}}{\sqrt{|\ell|}},\quad |\ell|\gg 1.$$

We now consider the terms involving $\mathbf{x}_{\ell m}^{(2)}$ and $\mathbf{x}_{\ell m}^{(4)}$. For $|\ell| \gg 1$, we have

$$H_0^{(1)}\left(\kappa_0\|\mathbf{x}-\mathbf{x}_{\ell m}^{(2)}\|\right)+H_0^{(1)}\left(\kappa_0\|\mathbf{x}-\mathbf{x}_{\ell m}^{(4)}\|\right)$$
$$\simeq\sqrt{\frac{1}{\mathrm{i}\pi\kappa_0|\ell|W}}\left[\mathrm{e}^{\mathrm{i}\kappa_0(2|\ell|W-(x_1+x_0))}+\mathrm{e}^{\mathrm{i}\kappa_0(2|\ell|W-(x_1-x_0))}\right],$$

and, for $|m| \gg 1$,

$$H_0^{(1)}\left(\kappa_0\|\mathbf{x}-\mathbf{x}_{\ell m}^{(2)}\|\right)+H_0^{(1)}\left(\kappa_0\|\mathbf{x}-\mathbf{x}_{\ell m}^{(4)}\|\right)$$
$$\simeq\sqrt{\frac{1}{\mathrm{i}\pi\kappa_0|m|H}}\left[\mathrm{e}^{\mathrm{i}\kappa_0(2|m|H-(x_2+y_0))}+\mathrm{e}^{\mathrm{i}\kappa_0(2|m|H-(x_2-y_0))}\right],$$

which leads to

$$R_\ell^{24}\simeq\frac{2}{\sqrt{\mathrm{i}\pi\kappa_0 W}}\cos(\kappa_0 x_0)\,\mathrm{e}^{-\mathrm{i}\kappa_0 x_1}\sum_{|\ell|=L}^{\infty}\frac{\mathrm{e}^{2\mathrm{i}\kappa_0|\ell|W}}{\sqrt{|\ell|}},\quad |\ell|\gg 1,$$

and

$$R_m^{24}\simeq\frac{2}{\sqrt{\mathrm{i}\pi\kappa_0 H}}\cos(\kappa_0 y_0)\,\mathrm{e}^{-\mathrm{i}\kappa_0 x_2}\sum_{|m|=M}^{\infty}\frac{\mathrm{e}^{2\mathrm{i}\kappa_0|m|H}}{\sqrt{|m|}},\quad |m|\gg 1,$$

respectively [36].

Combining these expressions together, we obtain

$$R_m\simeq 4\sqrt{\frac{\mathrm{i}\pi}{\kappa_0 H}}\,\mathrm{e}^{-\mathrm{i}\kappa_0 x_2}\cos(\kappa_0 y_0)\sum_{|m|=M}^{\infty}\frac{(-1)^m\mathrm{e}^{2\mathrm{i}\kappa_0|m|H}}{\sqrt{|m|}},\quad |m|\gg 1,|\ell|<L,$$

or

$$R_\ell\simeq 4\sqrt{\frac{\mathrm{i}\pi}{\kappa_0 W}}\,\mathrm{e}^{-\mathrm{i}\kappa_0 x_1}\cos(\kappa_0 x_0)\sum_{|\ell|=L}^{\infty}\frac{\mathrm{e}^{2\mathrm{i}\kappa_0|\ell|W}}{\sqrt{|\ell|}},\quad |\ell|\gg 1,|m|<M,$$

for the truncation error associated with the series representation of the Green's function. In either case, the series terms decrease like $1/\sqrt{|\ell|}$ or $1/\sqrt{|m|}$; hence, the truncation error decreases as the truncation order L or $M\to\infty$. We can therefore predict how many terms to take so that the series expansion of the Green's function satisfies its boundary conditions. Note that R_m is an alternating series while R_ℓ is not, therefore R_m is typically smaller in magnitude than R_ℓ. In other words, increasing M while fixing L does a better job at reducing the truncation error than increasing L while fixing M. Since L (resp. M) is associated with the x_1- (resp. x_2-) direction, these estimates are consistent with the fact that M must be large to accurately resolve the two different types of boundary conditions in the x_2-direction, i.e. the pressure release and reflecting boundary conditions at $x_2=H$ and $x_2=0$ respectively.

5. Numerical approximation

We consider an idealized situation where the bone specimen is a square of dimension $B\times B$. Because of this regular geometry, the domain is discretized into a uniform mesh consisting

of $N \times N$ points and a finite-difference scheme is used to solve the coupled system of equations (10), (11), (17) or (18), and (19)–(21).

More specifically, spatial derivatives in the bulk equations are approximated by 2nd-order centered difference formulas, while those in the boundary conditions are discretized by either backward or forward (2nd-order) formulas depending on the node's location. An exception is made for tangential derivatives along the boundary, which are approximated by the 1st-order backward formula. The reason for this is to promote diagonal dominance in the resulting linear system so that it is sufficiently well-conditioned to be solved numerically. Use of a 1st-order scheme involving only the nearest-neighbor nodes also helps keep the implementation relatively simple, especially near corners where a special treatment would be needed if large-stencil difference formulas were used. Because this switch from second to first order is restricted to tangential derivatives in the boundary conditions, it does not significantly affect the 2nd-order accuracy of the overall numerical scheme.

The quadrature of the boundary integrals in (17) or (18), and (20), (21) is performed via the trapezoidal rule. For example, equation (17) at node (i,j) on the left side of the square and away from the corners becomes

$$\begin{aligned}&\left(\lambda+2\mu-\frac{Q^2}{R}\right)\left[\frac{-3u_1(i,j)+4u_1(i+1,j)-u_1(i+2,j)}{2h}\right]\\&+\left(\lambda-\frac{Q^2}{R}\right)\left[\frac{u_2(i,j)-u_2(i,j-1)}{h}\right]+\left(1+\frac{Q}{R}\right)s(i,j)\\&=q\,G(\mathbf{X}_{ij},\mathbf{x}_0;\kappa_0)+h\sum_{\zeta_n\in\partial\Omega^b}G(\mathbf{X}_{ij},\zeta_n;\kappa_0)\varphi(\mathbf{x}_0,\zeta_n),\end{aligned}$$

or equivalently,

$$\begin{aligned}&\left(\lambda+2\mu-\frac{Q^2}{R}\right)\left[-3u_1(i,j)+4u_1(i+1,j)-u_1(i+2,j)\right]\\&+2\left(\lambda-\frac{Q^2}{R}\right)\left[u_2(i,j)-u_2(i,j-1)\right]+2h\left(1+\frac{Q}{R}\right)s(i,j)\\&-2h^2\sum_{\zeta_n\in\partial\Omega^b}G(\mathbf{X}_{ij},\zeta_n;\kappa_0)\varphi(\mathbf{x}_0,\zeta_n)=2h\,q\,G(\mathbf{X}_{ij},\mathbf{x}_0;\kappa_0),\end{aligned}$$

where h represents the uniform mesh size in the x_1- and x_2-directions. Note that the singularity at $\zeta_n=\mathbf{X}_{ij}$ for $\ell=0$ and $m=0$ in the Green's function G can be dealt with by approximating the Hankel's function $H_0^{(1)}(z)$ in the limit $z\to 0$, which then allows for an exact integration over the two subintervals adjacent to the singular point, yielding the contribution

$$\frac{4\mathrm{i}}{\pi}h\left[\log\left(\frac{h}{2}\right)-1\right],$$

in the boundary integrals.

We also point out that, since G is given by a double series (8) in this problem, its multiple evaluations for each pair of points $(\mathbf{x},\mathbf{x}_0)$ in the various boundary integrals take a substantial amount of CPU time, especially for large values of L and M. This is aggravated by the minimization procedure used for the recovery task (as discussed in section 6), which requires multiple evaluations of the equations and thus additional repeated evaluations of G. To overcome this difficulty, the Green's function is precalculated and saved for each pair $(\mathbf{x},\mathbf{x}_0)$ given L and M. In itself, this computation is also quite demanding in memory and CPU time but it is performed once for all before the code for parameter recovery is run. The saved values of G

are then simply called whenever they are needed in the evaluation of the equations. For the simulations presented in this paper, we prescribed terms up to $L = 200$ and $M = 200$ in the series of G. This choice was based on several trials, with L and M being large enough to ensure an accurate calculation of the Green's function.

The linear system resulting from the discretization of the equations is solved by a direct method such as Gaussian elimination. Note that the numerical solution includes the values of u_1, u_2, s and φ all together. Therefore, with a fine spatial resolution (i.e. large N), the size of this system is significant. For this reason, we only specified up to $N = 90$ mesh points in our simulations as this was deemed to be a good compromise between accuracy and computational cost. Keep in mind that the precalculation and storage of G also depends on N. Use of an iterative solver (e.g. GMRES) may be helpful in dealing with larger values of N but, because such a solver is not exact and produces errors that may affect the accuracy of parameter recovery, we eventually opted for a direct solver. This option is still reasonable in the present two-dimensional setting but, for potential three-dimensional applications, we anticipate that it would be necessary to consider an iterative solver.

Due to the large disparity in orders of magnitude among the various physical parameters, we find it is convenient to non-dimensionalize the equations for computations. This is accomplished by using the characteristic scales B (typically $B = 0.01$ m) and K_f as unit length and unit pressure, respectively. Accordingly, the dimensionless size of the bone sample is $B = 1$.

As an illustration, figures 2 and 3 show dimensionless profiles of u_1, u_2, s and φ for $W = 10$, $H = 10$, $B = 1$ and $\beta = 0.83$. Note that u_1, u_2 and s are defined in Ω^b while φ is only defined on $\partial\Omega^b$. In view of applications to the diagnosis of osteoporosis, we only pay attention to high bone porosities. We also restrict ourselves to low ultrasonic frequencies (250 and 500 kHz) because this falls within the range of frequencies that are typically used in medical applications and where Biot's theory is supposed to be applicable. On the other hand, the interrogating frequency should not be too low because otherwise it would not be able to resolve fine structures of cancellous bone. Earlier work by Buchanan *et al* [11] examined a similar problem via a finite-element approach but these authors only considered low frequencies up to 15 kHz because otherwise spurious resonances would affect their numerical solution. We did not experience such resonances in the present study.

6. Recovery results

6.1. Sensitivity tests

We first perform sensitivity tests to validate the model in preparation for the recovery task. After φ is obtained from solving the boundary value problem, the pressure P at any point in Ω^w can be determined via (16). In the present setup (figure 1), the bone specimen is centered at $(5B, 5B)$ and the point source is located at $\mathbf{x}_0 = (2B, 5B)$. The pressure is measured at 11 receiving points equally distributed between $2B \leqslant x_2 \leqslant 8B$ along the vertical axis $x_1 = 8B$. We also tried other configurations for the receiving points by varying their number and location but similar results were obtained, as already demonstrated in [27].

The objective function that we use for the sensitivity and recovery tests is the (relative) root-mean-square error

$$f(P_j^*, P_j) = \frac{\left[\sum_{j=1}^{11}(P_j^* - P_j)^2\right]^{1/2}}{\left[\sum_{j=1}^{11}(P_j^*)^2\right]^{1/2}}, \tag{29}$$

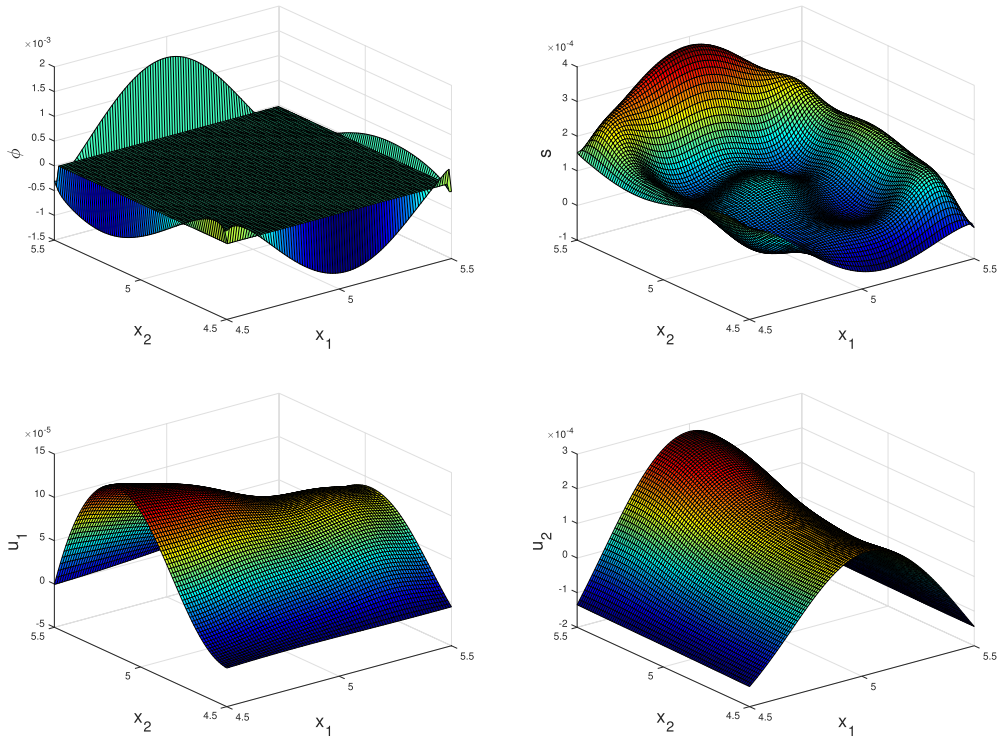

Figure 2. Profiles of φ, s, u_1 and u_2 for $\beta = 0.83$, $\omega = 250$ kHz and $N = 90$.

between a reference (or target) value P_j^* of the pressure field at each receiving point j and the corresponding trial value P_j. In laboratory experiments, P_j^* would refer to actual pressure measurements. Other physical parameters in our model are given the following values in dimensional SI units (see table 1): $\rho_f = 950$, $\rho_r = 1960$, $K_f = 2 \times 10^9$, $K_r = 2 \times 10^{10}$, $\eta = 1.5$, $\Lambda = 5 \times 10^{-6}$ and $\alpha_\infty = 1.05$ [23–26].

Focusing our attention on the determination of β, the sensitivity tests are performed by comparing a high-resolution ($N = 90$) target solution for a given value of β with lower-resolution ($N = 65$) trial solutions for a range of values of β. This comparison is based on a direct evaluation of the objective function (29), and is shown in figures 4 and 5 for $\omega = 250$ and 500 kHz. Such a test may be viewed as a convergence test for β with respect to the spatial resolution N.

Except for $\beta = 0.95$ with $\omega = 500$ kHz, the global minimum of (29) is found to occur near the target value of β in all cases being considered, as it should be expected. Note that $\beta = 0.95$ corresponds to very porous cancellous bone mostly made of saturated fluid (with a very sparse microstructure), therefore if a high frequency is used, the model may require a fine spatial resolution ($N \gg 90$) in order to produce an accurate computation. This may explain why poor results are obtained for $\beta = 0.95$ and $\omega = 500$ kHz with $N = 90$. The fact that the sensitivity curves for $\omega = 500$ kHz (figure 5) are more oscillatory in the high-porosity range further emphasizes the model's limitations when dealing with very high frequencies and porosities.

6.2. Univariate minimization

In view of potential applications to the diagnosis of osteoporosis, we now assess our model's ability to recover such parameters as β. The recovery tests consist in finding the value of β

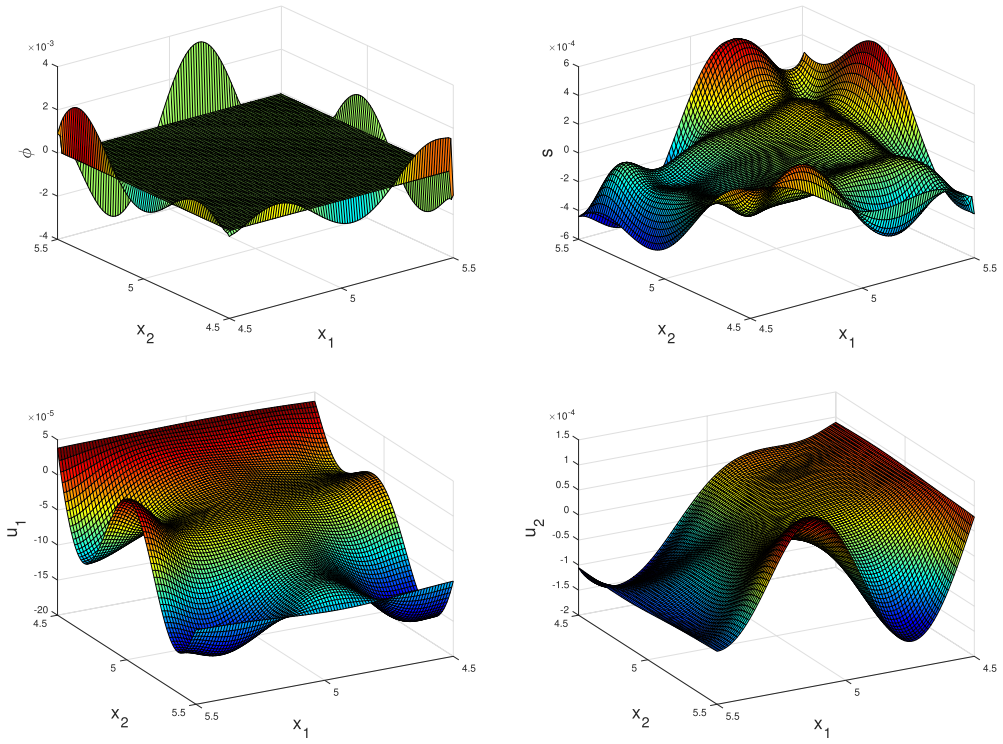

Figure 3. Profiles of φ, s, u_1 and u_2 for $\beta = 0.83$, $\omega = 500$ kHz and $N = 90$.

from the trial solution that minimizes the objective function (29) relative to a target solution with a prescribed value of β. Again, the target solution is taken to be of high resolution $N = 90$ while the trial solution has a lower resolution; three different trial cases $N = \{25, 45, 65\}$ are considered for each target choice.

Our minimization procedure is based on the Nelder–Mead (NM) simplex algorithm, which is denoted by the command *fminsearch* in Matlab. This rather standard method is certainly not the best performing one in the current literature, as its convergence may be slow depending on the choice of initial guess and there is no guarantee that it can find the global minimum of (29) for a given set of parameter values [12]. However, it is applicable to general nonlinear optimization problems and is relatively easy to implement as it does not require calculating any gradient of the objective function. Because the main goal of this study is to propose a suitable acoustic model that can serve as a basis for solving the inverse problem, regardless of any specific choice of minimization procedure, it is natural to conduct a preliminary analysis with the NM algorithm. As shown in this section and in the next ones, the NM method turned out to perform reasonably well in our recovery tests but it is our plan in the future to extend the present work by developing more sophisticated minimization strategies.

In this first recovery experiment, we aim to determine β alone, which is thus taken as the sole variable in the minimization procedure (hence the terminology 'univariate minimization'). For this purpose, other material parameters such as K_b and μ are approximated by explicit formulas in terms of β, namely

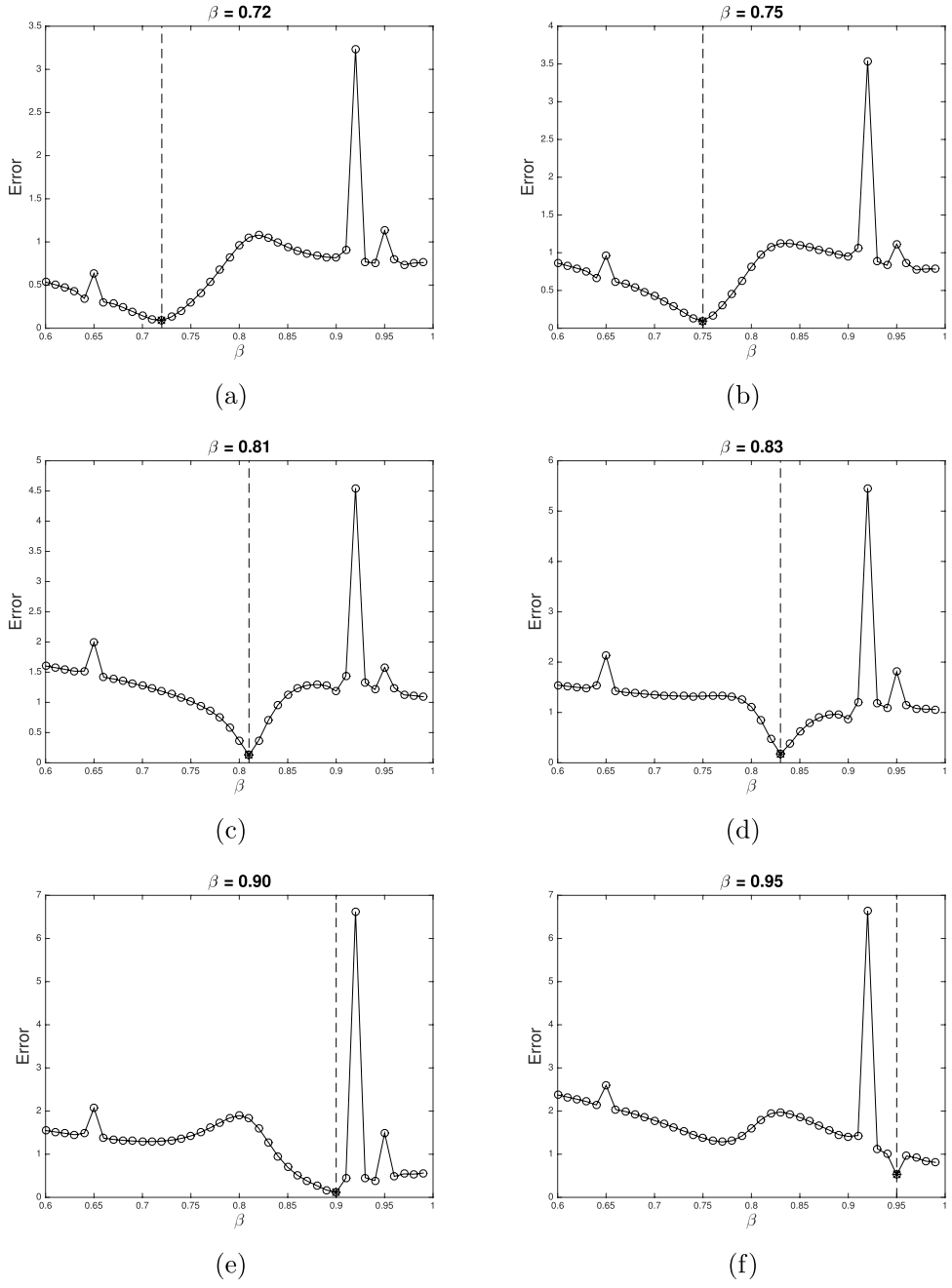

Figure 4. Sensitivity tests on β at $\omega = 250$ kHz with $N = 65$ and 90 for the low and high resolutions respectively. The vertical dash line represents the target value of β specified in the high-resolution solution. The black dot indicates the global minimum of the objective function.

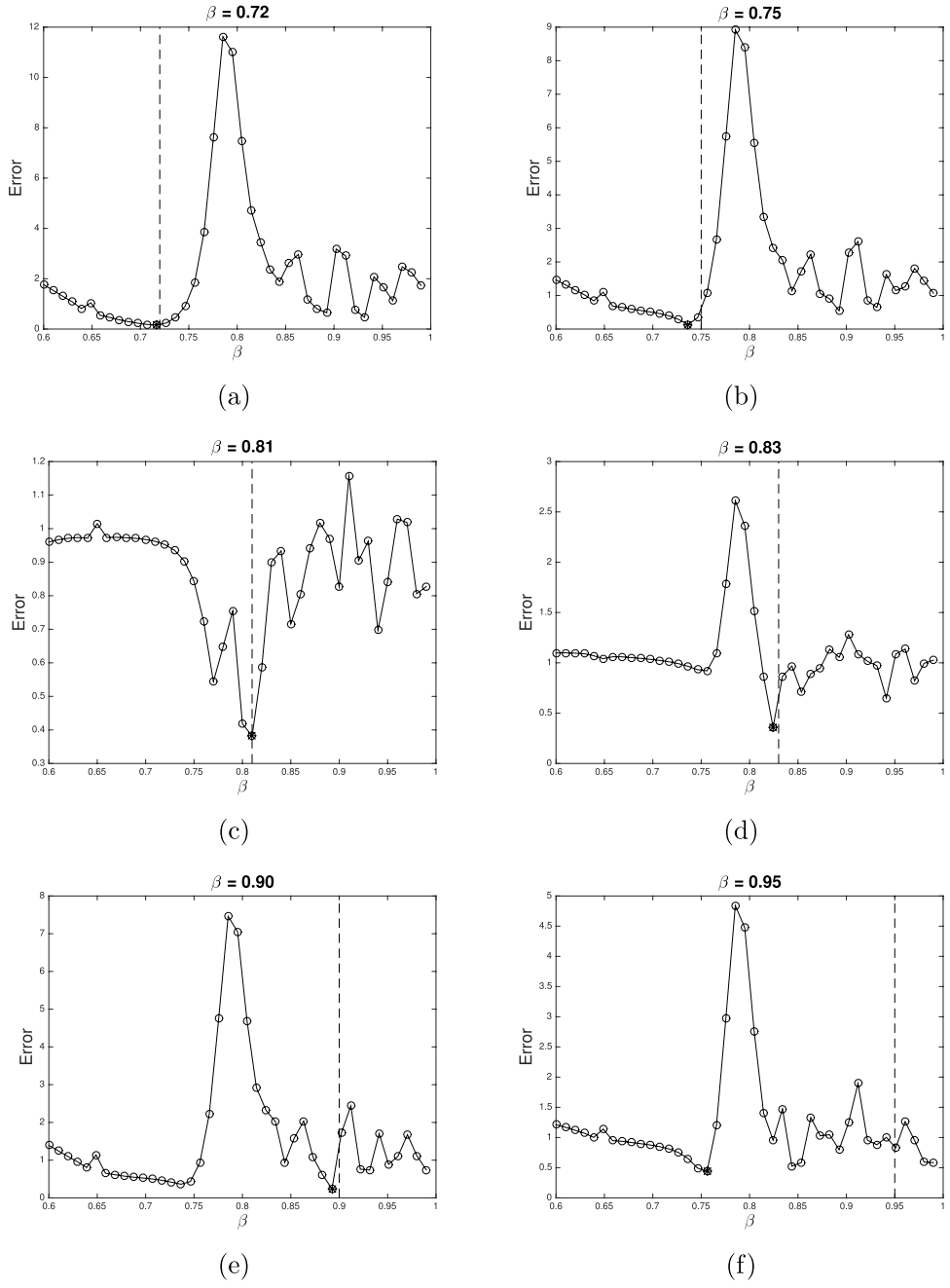

Figure 5. Sensitivity tests on β at $\omega = 500$ kHz with $N = 65$ and 90 for the low and high resolutions respectively. The vertical dash line represents the target value of β specified in the high-resolution solution. The black dot indicates the global minimum of the objective function.

Table 2. Errors on the recovery of β at $\omega = 250$ kHz for varying resolutions of the trial solution.

β	N	β	$f_{\min}$	Error
Target	Low/High	Recovered		%
0.72	25/90	0.7014	0.3247	2.5879
	45/90	0.7128	0.1849	1.0059
	65/90	0.7174	0.0887	0.3613
0.75	25/90	0.7357	0.3627	1.9043
	45/90	0.7452	0.2036	0.6348
	65/90	0.7484	0.0960	0.2148
0.81	25/90	0.7980	0.9406	1.4844
	45/90	0.8109	0.3507	0.1074
	65/90	0.8106	0.1242	0.0781
0.83	25/90	0.8888	0.9747	7.0898
	45/90	0.8322	0.4804	0.2637
	65/90	0.8306	0.1787	0.0684
0.90	25/90	0.9086	0.3982	0.9570
	45/90	0.8949	0.2092	0.5664
	65/90	0.8981	0.0828	0.2148
0.95	25/90	0.9725	0.7834	2.3730
	45/90	0.9482	0.0749	0.1880
	65/90	0.9472	0.3623	0.2917

- The real parts of K_b and μ are calculated using Williams' formulas [41]:

$$\begin{aligned} \mathrm{Re}K_b &= \frac{E}{3(1-2\nu)} V_f^n, \\ \mathrm{Re}\mu &= \frac{E}{2(1+\nu)} V_f^n, \end{aligned} \tag{30}$$

  where $V_f = 1 - \beta$ denotes the bone volume fraction. Following Hosokawa and Otani [30], we choose $n = 1.46$, $E = 2.2 \times 10^{10}$ and $\nu = 0.32$ for the exponent, Young's modulus and Poisson's ratio of solid bone respectively.
- The imaginary parts of K_b and μ are calculated using a log decrement ℓ:

$$\mathrm{Im}\overline{K_b} = \ell\,\mathrm{Re}\overline{K_b}/\pi, \quad \mathrm{Im}\mu = \ell\,\mathrm{Re}\overline{\mu}/\pi,$$

  with $\ell = 0.1$ as typically prescribed in underwater acoustics [13].

Tables 2 and 3 show recovery results for the same range of target values of $\beta = \{0.72, 0.75, 0.81, 0.83, 0.90, 0.95\}$ as depicted in figures 4 and 5. Again, both frequencies $\omega = 250$ and 500 kHz are used for the interrogation. The value $f_{\min}$ denotes the positive minimum of (29) that is attained after the NM algorithm has converged (the default stopping criterion was selected in *fminsearch*). As is typical in nonlinear optimization problems, the choice of initial guess is crucial for ensuring convergence to a suitable solution. It is usually desirable that the initial guess be chosen sufficiently close to a global minimum of (29). In the present case, given 'measured' data on the pressure field, we first perform sensitivity tests as done in section 6.1 (see figures 4 and 5) and then we select an initial guess for β that corresponds to the lowest point in the resulting curves. No *a priori* information on the target value of β is used

Table 3. Errors on the recovery of β at $\omega = 500$ kHz for varying resolutions of the trial solution.

β	N	β	$f_{\min}$	Error
Target	Low/High	Recovered		%
0.72	25/90	0.6527	0.3396	9.3457
	45/90	0.7055	0.3490	2.0117
	65/90	0.7147	0.1646	0.7422
0.75	25/90	0.8084	1.0147	7.7832
	45/90	0.7247	0.2692	3.3789
	65/90	0.7386	0.1210	1.5234
0.81	25/90	0.8186	0.6968	1.0645
	45/90	0.8052	0.6411	0.5957
	65/90	0.8053	0.3363	0.5762
0.83	25/90	0.8179	0.3300	1.4557
	45/90	0.8214	0.5398	1.0312
	65/90	0.8268	0.2998	0.3809
0.90	25/90	0.9448	0.3884	4.9756
	45/90	0.8880	0.1331	1.3381
	65/90	0.8947	0.0573	0.5884
0.95	25/90	0.9798	0.0948	3.1396
	45/90	0.9879	0.3298	3.9896
	65/90	0.9363	0.3155	1.4416

in this process. We checked that similar results are obtained by specifying slightly different values for the initial guess.

Overall, these results are found to be quite satisfactory, with errors on β being all under 10% and getting as low as 0.07%. This is comparable to the values obtained in [27] for an infinite water tank. The convergence with respect to N is clearly indicated for each target choice, i.e. both $f_{\min}$ and the errors decrease as N increases. The value of $f_{\min}$ gets below unity in all cases. Among the six target choices being considered, convergence is poorest for the most porous case $\beta = 0.95$, which is consistent with our earlier observations from the sensitivity tests. At the opposite end, the least porous case $\beta = 0.72$ exhibits significant errors for low resolutions but these errors quickly fall as N is refined. Among the two frequencies being used, recovery seems to be most accurate with $\omega = 250$ kHz, especially for porosities around $\beta = 0.8$. These results tend to confirm the expected regime of applicability of Biot's model, namely the interrogating frequency should not be too high and the interrogated material should be sufficiently porous (i.e. β should not be too low or too high).

6.3. Multivariate minimization

Motivated by these encouraging results on the single parameter β, we now follow up with an attempt to determine multiple parameters simultaneously. We restrict our attention to three parameters associated with bone strength, namely porosity β, frame bulk modulus $\mathrm{Re}K_b$ and frame shear modulus $\mathrm{Re}\mu$. Recall that, in the previous situation, $\mathrm{Re}K_b$ and $\mathrm{Re}\mu$ are defined as explicit functions of β by virtue of (30), but these formulas are mere approximations. We initially attempted to recover all three parameters simultaneously via a direct multivariate minimization of (29), but the results turned out to be unsatisfactory.

As an alternative, we first minimize (29) with respect to β alone, as described in the previous section, and then refine the calculation of $\mathrm{Re}K_b$ and $\mathrm{Re}\mu$. More specifically, after β has

Table 4. Errors on the recovery of $\mathrm{Re}K_b$ and $\mathrm{Re}\mu$ with $N = 65$ and 90 for the low and high resolutions respectively.

ω	$f_{\min}$	β	$\mathrm{Re}K_b$	$\mathrm{Re}\mu$
Target		0.72	3.18×10^9	1.30×10^9
250 kHz	0.0886	0.3613 %	3.4325 %	1.0033 %
500 kHz	0.1627	0.7422 %	15.0210 %	2.2596 %
Target		0.75	2.69×10^9	1.10×10^9
250 kHz	0.0960	0.2148 %	2.2365 %	0.8190 %
500 kHz	0.0818	1.5234 %	65.8171 %	5.9967 %
Target		0.81	1.80×10^9	7.38×10^8
250 kHz	0.1149	0.0781 %	159.6636 %	1.2445 %
500 kHz	0.0161	0.5762 %	13.6029 %	6.4212 %
Target		0.83	1.55×10^9	6.27×10^8
250 kHz	0.0811	0.0684 %	107.0513 %	2.0313 %
500 kHz	0.0544	0.3809 %	29.7124 %	12.1551 %
Target		0.90	7.06×10^8	2.89×10^8
250 kHz	0.0167	0.2148 %	35.8351 %	2.6764 %
500 kHz	0.0554	0.5884 %	17.7986 %	7.6404 %

been pinned down, only the other two parameters $\mathrm{Re}K_b$ and $\mathrm{Re}\mu$ are searched simultaneously, in which case both are taken as variables in *fminsearch*. Their initial guesses are given by (30) using the converged value of β to start the bivariate minimization procedure.

Table 4 shows the recovery results for target values corresponding to $\beta = \{0.72, 0.75, 0.81, 0.83, 0.90\}$ under illumination with frequencies $\omega = 250$ and 500 kHz. As an illustration, we take $N = 65$ and 90 for the low and high resolutions respectively, since their comparison yields the lowest errors on β among all the resolutions that we tested (see tables 2 and 3). The high-porosity case $\beta = 0.95$ is no longer considered given the rather poor results from the univariate minimization as indicated earlier. The multivariate computation would likely perform even worse in that situation. It is clear that accurate determination of additional parameters in this problem is dependent on a good guess for β, and therefore we should expect the corresponding errors to be higher than those on β.

The third column of table 4 reprints previous results on β as shown in tables 2 and 3; the fourth and fifth columns report the outcome of the bivariate minimization. It can be seen that we have some success at recovering $\mathrm{Re}K_b$ and $\mathrm{Re}\mu$. The recovery of $\mathrm{Re}\mu$ is especially good with errors of less than 8% in most cases, while the results for $\mathrm{Re}K_b$ are mixed depending on the frequency and porosity. Errors on $\mathrm{Re}\mu$ are uniformly small over the range of target values being considered, but they still indicate a slight preference for $\omega = 250$ kHz. On the other hand, using $\omega = 500$ kHz seems more adequate for retrieving $\mathrm{Re}K_b$. Indeed, errors on $\mathrm{Re}K_b$ are found to be less than 70% for all estimates at $\omega = 500$ kHz, while they get over 100% in some cases at $\omega = 250$ kHz. It is pointed out however that, unlike β, both $\mathrm{Re}K_b$ and $\mathrm{Re}\mu$ are characterized by very large absolute values. Therefore, despite the large errors found on $\mathrm{Re}K_b$, we are able to estimate this parameter within the typical range of orders of magnitude as spanned by its target values ($\sim 10^{-9}$–10^{-8}).

In addition to the NM algorithm, we also applied more sophisticated gradient-based optimization methods such as the interior-point (IP) and quasi-Newton (QN) algorithms (denoted respectively by the commands *fmincon* and *fminunc* in Matlab). In this case, the gradient of the objective function (29) was approximated numerically by finite differences. For convenience,

Table 5. Errors on the recovery of β with $N = 90$ for the trial solution. The target pressure is given by a semi-analytical solution [10].

ω	β	β	$f_{\min}$	Error
kHz	Target	Recovered		%
250	0.72	0.7824	0.1616	8.6621
	0.75	0.7843	0.2127	4.5703
	0.81	0.7860	0.3544	2.9590
	0.83	0.8283	0.2079	0.2051
	0.90	0.8228	0.6415	8.5742
	0.95	0.9072	0.9914	4.5047
500	0.72	0.6999	1.2827	2.7917
	0.75	0.7326	1.1866	2.3200
	0.81	0.8303	0.0025	2.5095
	0.83	0.8274	0.5064	0.3109
	0.90	0.7984	0.4422	11.2876
	0.95	0.8059	0.9401	15.1684

these results are not shown here because, despite the faster convergence, they turned out to be similar to those obtained with the NM algorithm.

6.4. Comparison with semi-analytical solution

We further test the recovering ability of our approach by specifying independent target data generated by an explicit semi-analytical solution for the pressure P^* in (29). In the simplified case where both the bone sample and water tank are of infinite extent in the vertical direction, the exterior pressure field for a time-harmonic point source can be expressed in a series form as derived by Buchanan and Gilbert [10] (see their equation 32). These authors solved Helmholtz's equation via contour integration of the Green's function and application of the residue theorem, producing a solution valid for high frequencies. The reader is referred to that paper for more details. This solution however requires finding the many complex-valued roots of $\Delta = 0$ where Δ is the determinant of an 8×8 matrix. This is an intensive computation that we performed numerically and validated against results in [10]. Note that the simpler Stoll approximation (rather than the Johnson approximation) was used for pore friction in [10]. However, this is not viewed as detrimental because it further contributes to independence of the two data sets being compared.

Table 5 lists the corresponding errors on the recovery of β alone. We again apply the NM algorithm to the minimization of (29) and use a high resolution $N = 90$ for the trial solution. In this test, to ensure a certain level of similarity in the geometric conditions while retaining the specificities of our numerical model, we only collect and compare data at a single location on the right side of the bone sample. This location is chosen to be at $\mathbf{x} = (8B, 5B)$ along the axis of vertical symmetry of the bone sample so as to minimize potential corner effects. As expected, errors are found to be overall larger than those obtained in the previous tests (see tables 2 and 3). However, most of them remain under 9%, which is quite acceptable. It is plausible that using a higher resolution in the numerical model would lead to more accurate results. As noted earlier, the largest errors occur for β near 0.95 with $\omega = 500$ kHz.

Following the procedure described in section 6.3, we also attempted to recover $\mathrm{Re}K_b$ and $\mathrm{Re}\mu$ via multivariate minimization of (29) relative to the semi-analytical solution for P^*. However, this investigation turned out to be rather unsuccessful as shown in table 6. Errors

Table 6. Errors on the recovery of $\mathrm{Re}K_b$ and $\mathrm{Re}\mu$ with $N = 90$ for the trial solution. The target pressure is given by a semi-analytical solution [10].

ω	$f_{\min}$	β	$\mathrm{Re}K_b$	$\mathrm{Re}K_b$	$\mathrm{Re}\mu$	$\mathrm{Re}\mu$
kHz		Target	Target	Error %	Target	Error %
250	0.0500	0.72	3.18×10^9	500.06	1.30×10^9	31.42
	0.1095	0.75	2.69×10^9	598.91	1.10×10^9	19.86
	0.5754	0.81	1.80×10^9	37.72	7.38×10^8	61.93
	0.5670	0.83	1.55×10^9	112.37	6.27×10^8	55.45
	0.6237	0.90	7.06×10^8	2.85×10^3	2.89×10^8	116.41
	5.85×10^{-9}	0.95	2.57×10^8	34.17	1.05×10^8	110.98
500	1.2794	0.72	3.18×10^9	43.52	1.30×10^9	10.90
	1.1663	0.75	2.69×10^9	85.23	1.10×10^9	4.53
	0.1614	0.81	1.80×10^9	34.56	7.38×10^8	19.21
	6.36×10^{-13}	0.83	1.55×10^9	14.39	6.27×10^8	16.92
	0.7891	0.90	7.06×10^8	680.97	2.89×10^8	11.36
	0.9773	0.95	2.57×10^8	3.87×10^3	1.05×10^8	3.98

on β are significantly amplified through the estimation of $\mathrm{Re}K_b$ and $\mathrm{Re}\mu$ and, although the results on $\mathrm{Re}\mu$ may still be deemed as acceptable, those on $\mathrm{Re}K_b$ are largely not. We did not see any improvement by employing the IP or QN algorithm, and we suspect this issue has more to do with our acoustic model due to its discontinuous dependence on K_b as suggested by the definitions of λ, Q and R in (4). Extension of our acoustic model is part of ongoing research and will be reported in a future publication. Alternatively, instead of directly estimating $\mathrm{Re}K_b$ and $\mathrm{Re}\mu$, one might simply use the approximate formulas (30) after β has been determined.

7. Conclusions

We have proposed a numerical model to recover material parameters of cancellous bone from acoustic measurements. This model is based on Biot's theory where cancellous bone is viewed as a poro-elastic material. A bone sample is illuminated by a signal of frequency ω from a point source located near one side and pressure measurements are taken at an array of receiving points located near the opposite side.

Compared to previous work [11, 22, 27], the present study considers conditions closer to an actual *in vitro* experiment. The bone sample is immersed in a finite water tank bounded above by a free surface, and high frequencies in the ultrasonic range ($\omega = 250$ and 500 kHz) are used for its acoustic interrogation. Biot's equations for cancellous bone are enriched with a more realistic dissipative term to allow for pore tortuosity. In view of potential application in the laboratory and potential extension as a diagnostic tool in clinical examinations, care is also taken to obtain an efficient and accurate numerical solution of the acoustic problem.

More specifically, to reduce the computational cost, a boundary integral approach was adopted to solve for the bounded fluid domain. This implies finding the corresponding Green's function and, for a two-dimensional rectangular tank, it can be written as an infinite double series in terms of Hankel's functions. Analytical results were established for the variational formulation of this nonlocal boundary value problem and its well-posedness, as well as for the asymptotic behavior of the series expansion of the Green's function to justify its truncation in numerical simulations. A finite-difference scheme was developed to solve Biot's

equations for the bone region, including boundary conditions that involve boundary integral equations defined along the boundary of the bone sample.

Numerical tests were conducted to assess our model's ability at recovering a number of Biot parameters. This is accomplished by minimizing an objective function representing the root-mean-square error between trial and target values of the pressure field. Target values were taken to be numerical values based on a well-resolved solution of our model, while trial values were obtained by using coarser resolutions. We were able to recover up to three Biot parameters (β, $\mathrm{Re}K_b$, $\mathrm{Re}\mu$) with satisfactory accuracy. Based on the univariate tests, we can determine bone porosity β to within 2% in most cases and within 0.07% in the best case. For the multivariate tests, we propose a simple recovery procedure where the objective function is minimized with respect to both $\mathrm{Re}K_b$ and $\mathrm{Re}\mu$ simultaneously, after first estimating β. This procedure was especially successful at determining $\mathrm{Re}\mu$, with errors as low as 0.8%, while the recovery of $\mathrm{Re}K_b$ turned out to be more highly dependent on the choice of ω. In the best case, $\mathrm{Re}K_b$ was found with 2% accuracy.

We have also performed a more careful assessment by using independent target data generated from a semi-analytical expression of the pressure field. In this case, the univariate and multivariate tests suggest that β and $\mathrm{Re}\mu$ may still be recovered with acceptable accuracy, yielding errors as low as 0.2% and 4% respectively. On the other hand, estimation of $\mathrm{Re}K_b$ proves again to be difficult with errors larger than 14%.

Overall, these results may be viewed as successful and support the potential use of this model as a theoretical basis in the development of acoustic techniques for assessing bone strength. The boundary integral formulation plays a central role in reducing the computational cost, thus making this model suitable for practical applications. Such an approach would be especially helpful in dealing with the three-dimensional problem as computations get even more intensive in this situation. On the other hand, our study also highlights limitations of Biot's theory and/or the recovery strategy. We have experienced difficulties in estimating $\mathrm{Re}K_b$ in general as well as β in the fluid limit (i.e. $\beta \simeq 1$). Ideally, we would like to test our model against actual laboratory measurements. We may also consider applying more sophisticated minimization methods than the NM, IP or QN algorithm, together with a better strategy to select initial guesses, in order to improve the calculations' accuracy or possibly be able to recover more than three Biot parameters. Another possible extension of this study would be to examine the inverse problem with heterogeneous Biot parameters [9]. These directions of inquiry are envisioned for future work.

Acknowledgments

This research was partially supported by the NSF through grant No. DMS-1615480.

ORCID iDs

Philippe Guyenne https://orcid.org/0000-0002-4199-3120

References

[1] Anderson C C, Bauer A Q, Holland M R, Pakula M, Laugier P, Bretthorst G L and Miller J G 2010 Inverse problems in cancellous bone: estimation of the ultrasonic properties of fast and slow waves using Bayesian probability theory *J. Acoust. Soc. Am.* **128** 2940–8

[2] Berryman J G 1981 Elastic wave propagation in fluid-saturated porous media *J. Acoust. Soc. Am.* **69** 416–24
[3] Biot M A 1956 Theory of propagation of elastic waves in a fluid-saturated porous solid. I. Lower frequency range *J. Acoust. Soc. Am.* **28** 168–78
[4] Biot M A 1956 Theory of propagation of elastic waves in a fluid-saturated porous solid. II. Higher frequency range *J. Acoust. Soc. Am.* **28** 179–91
[5] Biot M A 1962 Mechanics of deformation and acoustic propagation in porous media *J. Appl. Phys.* **33** 482–98
[6] Bonnet M and Constantinescu A 2005 Inverse problems in elasticity *Inverse Problems* **21** R1–50
[7] Bourbié T, Coussy O and Zinszner B 1987 *Acoustics of Porous Media* (Paris: Technip)
[8] Burridge R and Keller J B 1981 Poroelasticity equations derived from microstructure *J. Acoust. Soc. Am.* **70** 1140–6
[9] Buchanan J L and Gilbert R P 1997 Transmission loss in the far field over a one-layer seabed assuming the Biot sediment model *Z. Angew. Math. Mech.* **77** 121–35
[10] Buchanan J L and Gilbert R P 2007 Determination of the parameters of cancellous bone using high frequency acoustic measurements *Math. Comput. Model.* **45** 281–308
[11] Buchanan J L, Gilbert R P and Khashanah K 2004 Determination of the parameters of cancellous bone using low frequency acoustic measurements *J. Comput. Acoust.* **12** 99–126
[12] Buchanan J L, Gilbert R P and Ou M-J Y 2011 Recovery of the parameters of cancellous bone by inversion of effective velocities, and transmission and reflection coefficients *Inverse Problems* **27** 125006
[13] Buchanan J L, Gilbert R P, Wirgin A and Xu Y S 2004 *Marine Acoustics: Direct and Inverse Problems* (Philadelphia, PA: SIAM)
[14] Courant R and Hilbert D 1953 *Methods of Mathematical Physics* (*Interscience* vol 1) (New York: Interscience Publishers)
[15] Cowin S C and Nachlinger R R 1978 Bone remodeling III: uniqueness and stability in adaptive elasticity *J. Elast.* **8** 285–95
[16] Cowin S C and Van Buskirk W C 1979 Surface bone remodeling induced by a medullary pin *J. Biomech.* **12** 269–76
[17] Dunn K-J 1986 Acoustic attenuation in fluid-saturated porous cylinders at low frequencies *J. Acoust. Soc. Am.* **79** 1709–21
[18] Erdelyi A, Magnus W, Oberhettinger F and Tricomi F G 1953 *Higher Transcendental Functions* vol 2 (New York: McGraw-Hill)
[19] Fellah Z E A, Chapelon Y, Berger S, Lauriks W and Depollier C 2004 Ultrasonic wave propagation in human cancellous bone: application of Biot theory *J. Acoust. Soc. Am.* **116** 61–73
[20] Fry F J and Barger J E 1978 Acoustical properties of the human skull *J. Acoust. Soc. Am.* **63** 1576–90
[21] Geertsma J 1957 The effect of fluid pressure decline on volumetric changes of porous rocks *Trans. AIME* **210** 331–8
[22] Gilbert R P, Guyenne P and Hsiao G C 2008 Determination of cancellous bone density using low frequency acoustic measurements *Appl. Anal.* **87** 1213–25
[23] Gilbert R P, Guyenne P and Li J 2013 Simulation of a mixture model for ultrasound propagation through cancellous bone using staggered-grid finite differences *J. Comput. Acoust.* **21** 1250017
[24] Gilbert R P, Guyenne P and Li J 2013 A viscoelastic model for random ultrasound propagation in cancellous bone *Comput. Math. Appl.* **66** 943–64
[25] Gilbert R P, Guyenne P and Li J 2014 Numerical investigation of ultrasonic attenuation through 2D trabecular bone structures reconstructed from CT scans and random realizations *Comput. Biol. Med.* **45** 143–56
[26] Gilbert R P, Guyenne P and Ou M Y 2012 A quantitative ultrasound model of the bone with blood as the interstitial fluid *Math. Comput. Model.* **55** 2029–39
[27] Gilbert R P, Guyenne P and Shoushani M 2016 Recovery of parameters of cancellous bone by acoustic interrogation *Inverse Problems Sci. Eng.* **24** 284–316
[28] Gilbert R P, Hsiao G C and Xu L 2010 On the variational formulation of a transmission problem for the Biot equations *Appl. Anal.* **89** 745–55
[29] Grimes M, Bouhadjera A, Haddad S and Benkedidah T 2012 *In vitro* estimation of fast and slow wave parameters of thin trabecular bone using space-alternating generalized expectation-maximization algorithm *Ultrasonics* **52** 614–21
[30] Hosokawa A and Otani T 1997 Ultrasonic wave propagation in bovine cancellous bone *J. Acoust. Soc. Am.* **101** 558–62

[31] Hsiao G C and Wendland W L 2008 *Boundary Integral Equations* vol 164 (New York: Springer)
[32] Johnson D L, Koplik J and Dashen R 1987 Theory of dynamic permeability and tortuosity in fluid-saturated porous media *J. Fluid. Mech.* **176** 379–402
[33] Katz A J and Thompson A H 1986 Quantitative prediction of permeability in porous rock *Phys. Rev.* B **34** 8179–81
[34] Langton C M, Njeh C F, Hodgskinson R and Curey J D 1996 Prediction of mechanical properties of human cancellous bone by broadbeam ultrasonic attenuation *Bone* **18** 495–503
[35] McKelvie M L and Palmer S B 1991 The interaction of ultrasound with cancellous bone *Phys. Med. Biol.* **10** 1331–40
[36] Morse P M and Feshbach H 1953 *Methods of Theoretical Physics* part I (New York: McGraw-Hill)
[37] Nagy P B 1993 Slow wave propagation in air-filled permeable solids *J. Acoust. Soc. Am.* **93** 3224–34
[38] Plona T J 1980 Observation of a second bulk compressional wave in a porous medium at ultrasonic frequencies *Appl. Phys. Lett.* **36** 259–61
[39] Sebaa N, Fellah Z E A, Fellah M, Ogam E, Wirgin A, Mitri F G, Depollier C and Lauriks W 2006 Ultrasonic characterization of human cancellous bone using the Biot theory: inverse problem *J. Acoust. Soc. Am.* **120** 1816–24
[40] Stoll R D 1974 *Acoustic Waves in Saturated Sediments* (*Physics of Sound in Marine Sediments*) ed L Hampton (New York: Plenum)
[41] Williams J L 1992 Prediction of some experimental results by Biot's theory *J. Acoust. Soc. Am.* **91** 1106–12